Available online at www.sciencedirect.com

ScienceDirect

Acta Materialia 66 (2014) 32–43

Acta MATERIALIA

www.elsevier.com/locate/actamat

Size effects in bimetallic nickel–gold nanowires: Insight from atomic force microscopy nanoindentation

E.L. Wood [a], T. Avant [a], G.S. Kim [b], S.K. Lee [c], Z. Burchman [a], J.M. Hughes [d], F. Sansoz [a,e,*]

[a] Mechanical Engineering Program, School of Engineering, The University of Vermont, Burlington, VT 05405, USA
[b] Department of Semiconductor Science and Technology, Chonbuk National University, Jeonju 561-756, Republic of Korea
[c] Department of Physics, Chung-Ang University, Seoul 156-756, Republic of Korea
[d] Department of Geology, The University of Vermont, Burlington, VT 05405, USA
[e] Materials Science Program, The University of Vermont, Burlington, VT 05405, USA

Received 30 August 2013; received in revised form 21 November 2013; accepted 26 November 2013

Abstract

The crucial role that slip events emitted from free surfaces play in the overall plasticity and strength of low-dimensional crystals such as metallic nanowires (NWs) is well documented; however, the influences of stacking fault energy (SFE) and sample diameter on these local deformation processes are not clearly established. Experimental characterization by nanomechanical bending or tensile testing of NWs, in particular, may not be applicable to NWs made of different metals or exhibiting non-uniform dimensions. In this study, atomic force microscopy nanoindentation is used to probe the local plastic behavior and hardness properties of electrodeposited bimetallic Ni–Au NWs ranging from 60 to 358 nm in diameter and fixed on functionalized-glass substrates. Hardness measurements in individual NW segments are found to be larger in Ni than in Au owing to the difference in SFE and shear modulus between these two metals. However, the characteristic length scale associated with indentation size effects is shown to be material independent and directly linked to the NW diameter. Atomistic study of deformation mechanisms in single-crystalline NWs by molecular dynamics simulations further confirms that the interaction mechanisms between newly emitted dislocations and free surfaces are fundamentally different between Ni NWs and Au NWs during nanoindentation. By decoupling the intrinsic diameter dependence from indentation size effects in the hardness of bimetallic Ni–Au NWs, we find a marked reduction in size effects with a power-law scaling exponent of $n = 0.18$ during the incipient yielding of pristine NWs, in contrast to $n = 0.8$ in plastically pre-strained NWs.

Keywords: Atomic force microscopy (AFM); Nanowire; Nickel; Gold; Nanoindentation

1. Introduction

In the last decade, a large number of applications employing single-crystalline nanowires (NWs) have been realized for storage [1,2], sensors [3–6], gene therapy [7] and self-assembled devices [8]. Progress in NW synthesis has made possible the design of heterojunctions with two or more metals in a variety of motifs such as core–shell, crown-jewel and barcoded NWs, lending themselves for breakthroughs in catalysis [9], immunoassays [10] and optical tags [11]. Likewise, bimetallic or striped NWs have been of particular interest as multiplexing detection systems [12,13].

It is well established that the functional properties of low-dimensional metallic materials are strongly size dependent, e.g. the absorption of light by Au nanoparticles [14]; however, gaining a fundamental understanding of the size effects in plastic deformation of geometrically confined metals remains an important

* Corresponding author at: Mechanical Engineering Program, School of Engineering, The University of Vermont, Burlington, VT 05405, USA. Tel.: +1 802 656 3837; fax: +1 802 656 3332.
E-mail address: frederic.sansoz@uvm.edu (F. Sansoz).

1359-6454/$36.00
http://dx.doi.org/10.1016/j.actamat.2013.11.067

challenge. Surface-mediated dislocation nucleation has been shown to govern the plasticity in ultrathin metallic NWs in computer simulations [15–24] and nanoscale experiments [25–31]. Past atomistic simulation studies have predicted that surface-mediated plasticity is generally localized and strongly dependent on the NW diameter [32,33], the surface morphology [18,34,35] and the stacking fault energy (SFE) curve [36,37]. Yet, these simulations rely on semi-empirical interatomic potentials, whereas direct experimental evidence of SFE and size effects on surface dislocation dynamics in NWs remains limited.

Furthermore, significant advances have been made in mechanical testing of low-dimensional nanostructures, such as nanomechanical tensile testing [28,38–45], nanocolumn compression [46–50] and NW bending [51–53]. Although these techniques are useful to gain quantitative insight into the mechanical behavior of single-crystalline NWs, they are not well suited for charac terization of mechanical properties in NWs with different metals, such as bimetallic NWs, or exhibiting non-uniform dimensions. Conversely, nanoindentation [54], which has been used extensively to investigate size-dependent plasticity in metallic thin films [55–58] and other patterned quasi-one-dimensional metals [59–63], offers a unique advantage for characterization of bimetallic NWs by enabling local measures of plastic behavior in reduced specimen areas. However, nanoin dentation of crystalline metals notoriously gives rise to indentation size effects (ISEs) [64] that make intrinsic sample size effects more difficult to analyze in metallic NW studies. Furthermore, there is a growing body of evidence confirming that hardness properties are diameter dependent in metallic NWs and nanopillars [65–67], though the role of SFE on underlying plasticity mechanisms is still not fully understood.

This study presents a successful attempt to decouple ISE and diameter effects in the hardness and plasticity of electrodeposited bimetallic NWs by pairing AFM nanoindentation experiments with atomistic simulations. Our combined experimental–atomistic simulation approach is deployed to examine the role of SFE in bimetallic NWs varying between 60 and 358 nm in diameter and constructed with segments of Ni and Au, two face-centered cubic (fcc) metals with very different stacking fault energies, 124 and 42 mJ m^{-2}, respectively [36]. Details of the methods are provided in Section 2. Section 3 presents the structure of electrodeposited bimetallic Ni–Au NWs and the hardness of individual NW segments as a function of contact depth and NW diameter. This section also presents the results of atomistic simulations aimed at understanding the effects of crystal orientation and SFE on slip activity in single-crystalline Ni and Au NWs subjected to AFM nanoindentation. The influence of SFE and plastic straining on size effects in bimetallic Ni–Au NWs is discussed in Section 4.

2. Materials and methods

2.1. Nanowire fabrication

Bimetallic NWs containing two Ni–Au heterojunctions were created by electrodeposition into the pores of an anodized aluminum oxide (AAO) sacrificial template using a previously published method [68]. 50 μm thick AAO membranes with nominal pore sizes of 200 nm, 100 nm (Whatman plc, Maidstone, UK) and 55 nm (Synkera Technologies, Inc., Longmont, CO) were used in this study. An electrode was formed by sputter coating of a thin Au layer (<100 nm) on the membrane side exhibiting the smallest pore size (we note here that the pore shape in these membranes was found to be slightly conical). Ni segments were obtained with a standard Watts bath (Transene, Danvers, CO) at 55 °C against a 99.995% pure Ni electrode (Alfa Aesar, Ward Hill, MA) at a voltage of −1 V. These conditions were found to produce single-crystalline NWs in the existing literature [69]. After Ni deposition, the template was immersed in a deionized (DI) water solution at room temperature, followed by several DI water rinses to wash away the electrolyte solution. A commercially available Au plating solution, Orotemp-24 (Technic, Inc., Cranston, RI), was used as a bath for deposition of Au segments. A platinized titanium mesh (Rolling Thunder Pyrotechnics, Rhinelander, WI) was used as anode with a deposition voltage of −0.7 V [68]. Following this step, the template was again rinsed several times and placed back into the Watts bath under the conditions described above, with care taken to not overplate the template. The times of electrodeposition were equal to 20 and 45 min for Ni and Au segments, respectively. Pure Ni NWs were also made to serve as a control.

The NWs were freed by dissolving the template in 25% sodium hydroxide (Alfa Aesar, Ward Hill, MA). The precipitate was collected at the bottom of a vial placed on top of a magnet, and washed several times with DI water followed by several washes in ethanol. The NWs were subsequently stored in pure ethanol. The NWs were characterized by tapping-mode topographical atomic force microscopy (AFM), scanning electron microscopy (SEM) using either secondary or backscattered electron imaging, and scanning transmission electron microscopy (STEM) with energy-dispersive spectroscopy (EDS). X-ray diffraction (XRD) patterns were also acquired with a Rigaku MiniFlex II using a Cu K_α radiation. XRD was performed both on bimetallic NWs left in an AAO template, which had been partially etched to expose the NW tips, and on NWs released from the template and dispersed on a flat amorphous substrate to produce powder XRD patterns.

2.2. AFM nanoindentation

Pure Ni NWs were drop-casted on a Si (1 1 1) wafer and aligned with a magnet before being allowed to dry in air.

Bimetallic NWs were drop-casted on an amino-silanized glass (Sigma–Aldrich, St Louis, MO), taking advantage of the amine–aurophilic [70] interaction (Fig. 1a) to mitigate the possibility of the NW rolling away upon scanning or indentation. Quantitative hardness measurements were carried using a universal scanning probe microscope with a *XYZ* closed-loop scanner (Quesant, Santa Cruz, CA). Following the manufacturer's calibration procedure, positioning precisions of 6.5, 9.6 and 0.1 nm were measured along the X, Y and Z directions, respectively, for a maximum XY scan size of $40 \times 40\ \mu m^2$ and a vertical Z range of 6.11 μm. The atomic force microscope was fitted with a cube-corner diamond probe glued on a sapphire AFM cantilever (both the cantilever and the tip were assembled by Micro Star Technologies, Huntsville, TX). The cube-corner tip was scanned over a TGT1 grating with sharp silicon spikes in order to obtain a three-dimensional (3-D) image of the tip. Using the tip identification package in the software SPIP, it was determined from this 3-D image that the tip apex was 74.5 nm in radius with an half angle of 44.8°. The 3-D image was also used to fit an area function associated with the diamond probe, $A_c = f(h_c)$, where h_c is the distance for the tip apex, i.e. equivalent to the contact depth in the following, and f is a second-order polynomial function. The cantilever spring constant was found equal to $k = 906.4\ \mathrm{N\ m^{-1}}$ by linear elastic finite-element analysis [71]. The force–voltage relation was calibrated before each new nanoindentation series by using the force-matching method [71] with a polished fused-quartz substrate. Extreme care was taken to ensure that there was no movement of the laser and detector in the AFM head when exchanging the calibration standard for the specimens covered by NWs.

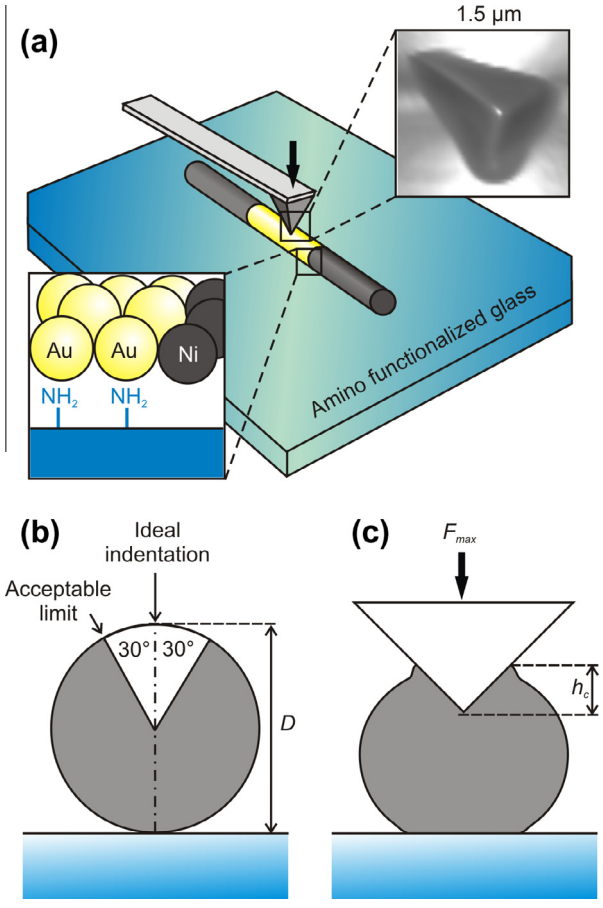

Fig. 1. AFM nanoindentation of bimetallic Ni–Au NWs. (a) Schematic of experimental nanoindentation setup showing a bimetallic NW with Au segment fixed to an amino-functionalized glass slide. Inset on the right-hand side shows a 3-D AFM image of the indenter tip obtained by scanning on a TGT1 Si grating. Illustration of NW cross-section (b) showing regions of acceptable and unacceptable indentations and (c) during deformation up to a contact depth h_c.

A schematic of the AFM nanoindentation setup developed in this study is shown in Fig. 1a. The nanoindentation procedure on NWs was carried out as follows. The substrate was scanned with a rate between 0.5 and 0.75 Hz at a resolution of 300 lines. After locating a single NW, a 2 μm × 2 μm scan was performed on an area of interest such that the symmetry axis of the cube-corner diamond probe was parallel to the NW axis. The AFM was then allowed to rest for at least 10 min, after which the area was scanned again to ensure that no significant creep effect was present. The bare substrate and the NW were indented subsequently by displacing the piezo-scanner toward the diamond tip at a constant rate of $1\ \mu m\ s^{-1}$, leading to a loading rate of $\sim 10\ \mu N\ s^{-1}$, until a desired force was attained. In this study, the maximum applied force for nanoindentation F_{max} varied between 15 and 40 μN. Each indentation was ideally performed at the maximum height of the NW shown on the AFM scan (Fig. 1b). However, slight offsets as far as 30° from the NW apex were found to be acceptable in measuring the contact depth h_c. Here, h_c corresponds to the residual depth obtained by post-indentation AFM imaging after the diamond probe was withdrawn, and was determined by measuring the height difference across the indentation with the grain measurement analysis in the software Gwyddion [72] (Fig. 1c). We assumed that the difference between contact depth and residual depth was negligible for shallow indentations [71]. The contact area A_c was calculated using the measured h_c value, and the local hardness H was obtained from the equation:

$$H = \frac{F_{max}}{A_c}. \quad (1)$$

It is worth noting that using the value of h_c to calculate A_c is valid, despite any differences in the geometry of the plastic indent (Fig. 3b and e) [71].

2.3. Molecular dynamics simulation

Molecular dynamics (MD) simulations of plastic deformation in fcc NWs deformed by nanoindentation were performed with the software LAMMPS (Large-scale Atomic/Molecular Massively Parallel Simulator) following the methodology in Ref. [65]. All atomistic models were single crystalline with a perfect circular cross-section and no heterojunction. The diameter and length of the NW were 30 and 40 nm, respectively. Periodic boundary conditions

were applied along the NW axis. We made use of the embedded-atom-method (EAM) interatomic potentials formulated by Mishin et al. [73] and Grochola et al. [74] to simulate Ni and Au atoms, respectively, because their parameters have been fitted on ab initio data to predict stacking-fault and surface energies accurately, compared to experimental data [36]. As shown below, experimental NWs were preferentially grown with either a [1 1 1] or [0 0 1] axis, which also represented the axes considered in our atomistic models. For [1 1 1]-oriented NWs, models with five different NW tilt angles varying from 0° to 60° with respect to the $[1\,1\,\bar{2}]$ crystallographic direction were investigated. The crystal orientations of 0°-tilt NWs were the same as in Ref. [65], i.e. $x = [\bar{1}\,1\,0]$, $y = [1\,1\,\bar{2}]$ and $z = [1\,1\,1]$, where y is the loading direction and z is the direction parallel to the NW axis. For [0 0 1]-oriented NWs, the crystal orientations were fixed with no tilt rotation, and equal to $x = [1\,0\,0]$, $y = [0\,1\,0]$ and $z = [0\,0\,1]$. The tip was simulated by exerting a spherical repulsive force on each surface atom with a force constant of $10\ \mathrm{N\,m^{-2}}$. A tip radius of 9 nm was chosen to approximately match the ratio of tip radius over NW diameter used in experiments, ~0.3. The tip surface was positioned at 0.2 nm from the NW surface at the start of simulation, and moved toward the wire at a rate of $1\ \mathrm{m\,s^{-1}}$. Before deformation, the NWs were relaxed with an energy minimization at 0 K using a conjugate gradient algorithm, followed by a zero-force relaxation at 300 K for 50 ps using constant number of particles, volume and pressure (NPT) through a Nosé–Hoover thermostat. Indentation was performed at 300 K with constant number of particles, volume and temperature (NVT). The time step was 5 fs. The bottom two atom layers were constrained by zeroing out atomic forces and velocities in all directions in order to prevent the wire from rolling and sliding. The simulations were run for 2 ns (400,000 steps), resulting in a contact depth of 1.8 nm. Visualization of atomic-scale deformation was performed by using the local crystal structure analysis of Ackland and Jones [75]. In the following, all atoms in fcc arrangement are omitted for clarity. The nanohardness in the simulation was calculated from the mean contact pressure p_m, defined as:

$$p_m = \frac{P}{A_p}, \tag{2}$$

where P is the total force applied parallel to the loading direction, and A_p is the projected contact area calculated from atomic positions using the method described in Ref. [76].

3. Results

3.1. Nanowire characterization

The bimetallic NWs synthesized in this study were found to be between 16 and 18 μm long, with some areas of branches or irregular diameters due to imperfect pores in the template, as shown in Fig. 2a. Backscattered electron SEM imaging revealed brighter sections in the middle of the NWs compared to the ends, which made it possible to identify Au segments of ~6 μm in length sandwiched between two Ni segments of equivalent size.

The XRD pattern of vertically aligned bimetallic NWs embedded in the sacrificial template is shown in Fig. 2b. This spectrum displays strong Au(1 1 1) and Au(2 0 0) reflections, a moderate Ni(2 0 0) reflection and a weak Ni(2 2 0) reflection. The powder XRD pattern of freed NWs (not shown) revealed a lack of Ni(2 0 0) reflection at 51.8°, which conversely points to Ni segments with a preferential (2 0 0) growth direction. It is also important to note that the Au(2 0 0) and Ni(1 1 1) reflections are close in theory at $2\theta = 44.38°$ and 44.5°, respectively, and thus could likely overlap in our spectrum. Therefore, this analysis suggests that the NW segments were single crystalline with a preferential growth parallel to either [1 1 1] or [0 0 1] crystallographic directions in both Au and Ni segments. However, we remained cautious that other NW orientations may have been possible in AFM nanoindentation of individual NW segments, because their crystal structure could not be directly ascertained by AFM imaging.

Furthermore, we observed that NWs released from the template exhibited several bent Au segments (Fig. 2c), possibly due to the NWs being placed in an ultrasonic cleaner to break up any cluster, or to the drop-casting of the NWs on the substrate. In addition, a few Au segments were also found to be broken near the Ni–Au heterojunction. The EDS analysis confirmed that heterojunctions were clearly defined, as shown in inset of Fig. 2c, with little mixing of metals across the Ni–Au interfaces (Fig. 2d).

3.2. Experimental hardness

A total of 41 individual indentations were performed including seven indents on pure Ni NWs with three NWs each being indented one time and one NW being indented four times with each indent no closer than 1 μm. The remaining indents were obtained across different bimetallic NWs. A single bimetallic NW was typically indented at each end and in the middle to capture the plastic response of both metals. Because of the deposition motif, indents near the ends were most likely, though not necessarily, Ni. Identification of the metal was therefore verified using other factors: the indent appearance, the local hardness, and the shape of the loading and unloading curves, as explained below. Of the 34 indents performed on bimetallic materials, 24 were identified to be from Au segments. Fig. 3 presents the representative AFM images of indentations in Au and Ni segments obtained with the same applied force, ~35 μN. The corresponding height profiles in Fig. 3c and f show that permanent deformation and pile-ups near the indents were more clearly visible in Au segments than in Ni ones. This result was found to be in line with the shape of the loading–unloading curves in Fig. 3g, showing that a

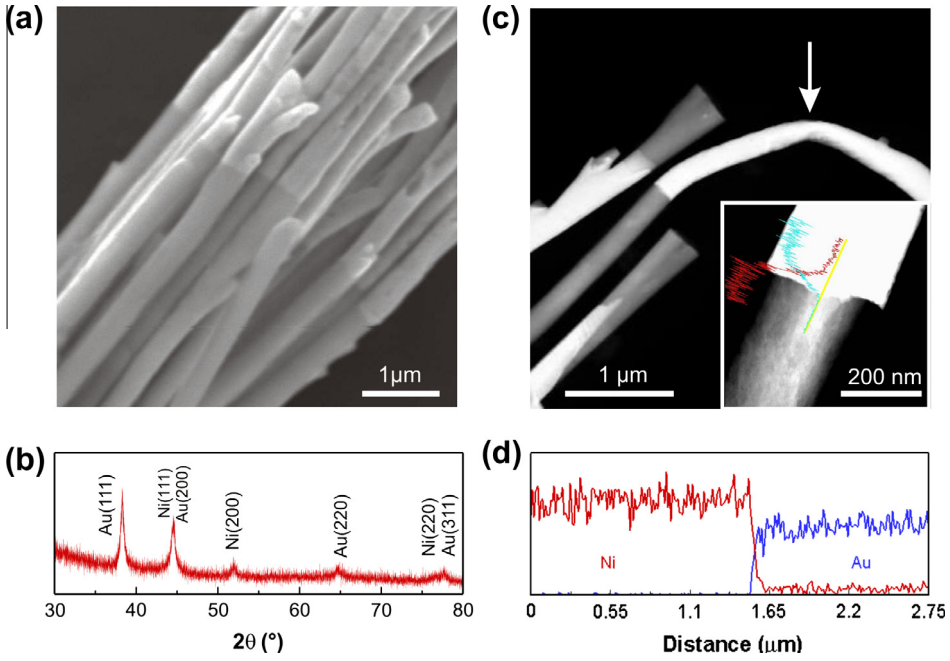

Fig. 2. Bimetallic Ni–Au NWs obtained by template-assisted electrodeposition. (a) Backscattered-electron SEM image of a bimetallic NW bundle. (b) XRD pattern of electrodeposited bimetallic NWs inside the sacrificial AAO template. (c) STEM image of Ni and Au segments. Arrow points to a bent Au segment deformed during synthesis. Inset: Close-up view of a Ni–Au heterojunction. (d) EDS profiles for Ni and Au atom content showing no significant atomic diffusion at the Ni–Au interface.

larger plastic work was dissipated in Au segments than in Ni segments.

All hardness measurements from this work are presented in Fig. 4a as a function of the contact depth h_c normalized by the local diameter measured at the indentation site (Fig. 1b). We found that Au segments had an average hardness of 2.84 GPa with a standard deviation of ±0.68 GPa for indentation forces of between 17.1 and 39.27 μN. In contrast, Ni segments proved to be much harder with an average hardness of 12.57 GPa; however, Fig. 4 also shows a larger standard deviation ±4.91 GPa for a similar range of forces. This finding suggested a difference in size effects between Ni and Au NW segments, although it was not clear at this stage of analysis whether this difference resulted from extrinsic ISE or intrinsic diameter effects.

Moreover, Fig. 5 presents the effect of material aging on the nanohardness of Ni NW segments over the course of several years. This figure clearly shows that the hardness was not sensitive to aging. Hence these experimental results ruled out the hypothesis that the nanoindentation of Ni segments was influenced by the growth of an oxide shell, if any. This also confirms that the structure of the bimetallic Ni–Au NWs was very stable.

3.3. Atomistic simulations of deformation processes and hardness

Atomistic snapshots of the dislocation dynamics during the nanoindentation of single-crystalline [1 1 1]-oriented Ni and Au NWs are shown in Fig. 6. The force–displacement curves corresponding to these simulations (Fig. 7a) indicate that the NWs behaved elastically until the occurrence of discrete yielding steps resulting from sharp drops in contact force. Geometrically necessary dislocations (GNDs) were found to expand under the spherical tip with the increase in contact area; however, their role on the mechanical response was considered to be inconsequential because they occurred prior to the first yielding step in Fig. 7a. The relevant yielding mechanism in [1 1 1]-oriented Ni NWs was found to correspond to the emission of prismatic dislocation loops in the contact zone, followed by their escape from the crystal on the opposing surface at the bottom of the NW (Fig. 6a, d and Movie S1). Each of these single-slip events led to a marked decrease in mean contact pressure, as shown in Fig. 7b. By way of contrast, the plastic deformation of Au NWs was found to differ from the interaction mechanism between newly emitted loops and the free surface predicted in Ni NWs. In this case, incipient plasticity resulted from the growth of GNDs into spiral dislocations, which were quickly absorbed by the surface close to the tip after one or two rotations (Fig. 6d and f). This yielding process did not produce any plastic deformation at the bottom of the Au NWs, as opposed to that predicted in Ni NWs (Fig. 6h and g, respectively).

In addition, the simulated nanoindentation of [0 0 1]-oriented NWs showed a change in elastic response at shallow contact depths, but proved to exhibit no significant difference in plastic deformation mechanisms and the yielding contact pressure required to emit the first dislocations

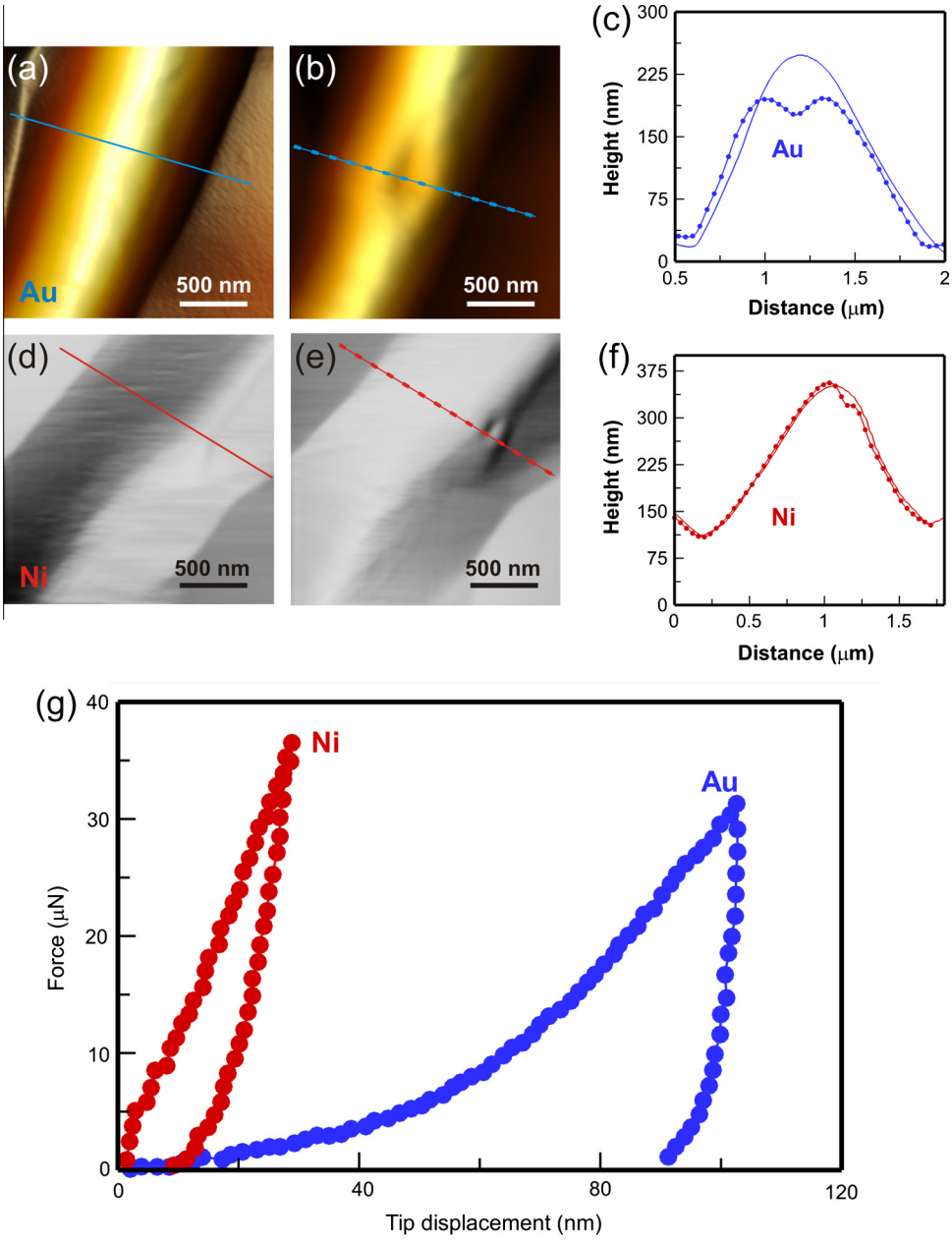

Fig. 3. Representative nanoindentation response of Ni and Au segments in bimetallic NWs. AFM images and line profiles obtained before and after indentation in (a)–(c) Au NW segment and (d)–(f) Ni segment. (g) Force–displacement curves for the indents shown in (b) and (e).

(Fig. 7c). Furthermore, testing the effect of loading direction with different NW tilt angles, which is relevant to the interpretation of AFM nanoindentation experiments, allowed us to conclude that the NW rotation also had little influence on the yielding contact pressure and deformation mechanisms in [1 1 1]-oriented Au NWs and Ni NWs, except for the Ni NW with a 30° tilt angle resulting in a higher yield point (Fig. 7d). It is worth noting, however, that for the Ni NW with 30° rotation, newly emitted dislocation loops were blocked by the fixed boundary in the lower part of the NW, and found to remain in the crystal; thereby increasing in yield contact pressure. Similarly, several dislocation arms were predicted to be pinned at the bottom boundary in Au NWs after large plastic deformation, suggesting the possible accumulation of crystal defects in AFM experiments on heavily deformed Au NWs. Furthermore, Fig. 4a shows good hardness agreement between the predictions from atomistic simulations and the experimental measurements from AFM nanoindentation. This result is surprising considering that the strain rates are different by several order of magnitudes, but not uncommon because this phenomenon has also been observed previously by Sansoz and Stevenson [77] in the AFM nanoindentation of nanocrystalline Ni films. Fig. 4a also shows that the data in Au NW segments were collected with much larger normalized contact depths in

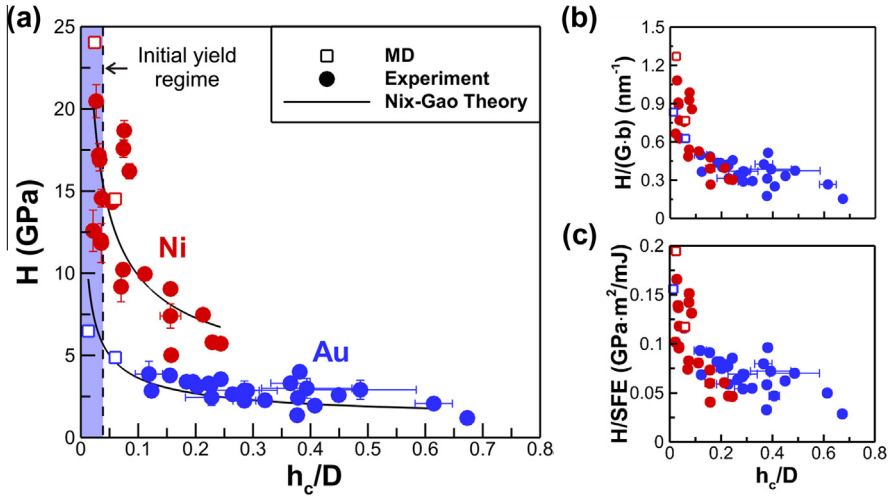

Fig. 4. Nanoindentation size effects. (a) Hardness vs. normalized contact depth obtained in Ni and Au segments where D is the NW diameter. Nix–Gao theory from Eq. (3) with $h^* = D$ is shown using $H_0 = 2.97$ and 1.09 GPa as fitting parameters in Ni and Au, respectively. An estimate of the initial yield regime based on the onset of plasticity predicted by MD simulation is indicated by a shaded area. Hardness of Ni and Au NWs normalized by (b) the product of shear modulus G and magnitude of Burgers vector b, and (c) the SFE as a function of normalized contact depth. In each figure, error bars include measurement uncertainties for both the contact depth due to pile-ups and the NW diameter.

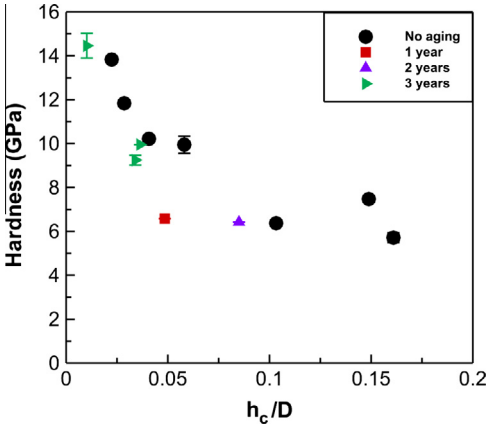

Fig. 5. Influence of room-temperature aging and oxidation in air on hardness of Ni NW segments as a function of normalized contact depth. Aging effects on the nanoindentation response are found to be negligible.

experiments compared to those from simulations, while some experimental and simulation data tend to overlap in Ni NW segments.

4. Discussion

4.1. Data interpretation in nanoindentation of NWs on flat substrates

Although traditional depth-sensing instrumented indentation on flat substrates is a well-established technique, AFM nanoindentation of metallic NWs on flat substrates requires special attention. Because nanoindentation experiments are force controlled, the interpretation of total displacements in NW indentation remains a major challenge. This is due to the strong non-linearity from the double-contact deformation at the tip–NW and NW–substrate interfaces [60], as well as from the lateral elastic expansion of the NW because of free surfaces [78]. Also, considerations on how the NW is anchored to the substrate are of critical importance. Past theoretical studies have proved that free or fixed-end boundary conditions can directly influence the force–displacement nanoindentation response [60,79]. Also, the AFM nanoindentation setup used raises a question about the role of amine–aurophilic interaction at the NW–substrate interface. The mechanics for this type of interaction is not fully understood and challenging to quantify experimentally, but also proves to play a key role in preventing the NWs from rolling in our AFM nanoindentation experiments. As a result of these above limitations, we were not able to measure the elastic properties of the NW segments, despite our predictions that the elastic behavior of the NWs varies with the NW orientation, as shown in Fig. 7b and c. Nonetheless, two unique features of AFM nanoindentation were deployed for the characterization of incipient plasticity in bimetallic NWs. First, non-contact high-resolution imaging of surface areas in AFM nanoindentation provided accurate tip positioning prior to indentation, along with a rapid account of permanent deformations after testing. In Fig. 3, qualitative differences in terms of plastic deformation processes have been observed between Au NW segments and Ni NW segments. This agrees well with our atomistic simulations showing in Fig. 6 that the interaction mechanisms between newly emitted dislocations and free surfaces are fundamentally different between Ni NWs and Au NWs during nanoindentation. Second, recent progress in AFM nanoindentation protocol using diamond probes mounted on AFM cantilevers has been shown to reduce the error in force measurement down to 2%, compared to 37% using the standard protocol [71]. Therefore, the hardness measurement errors

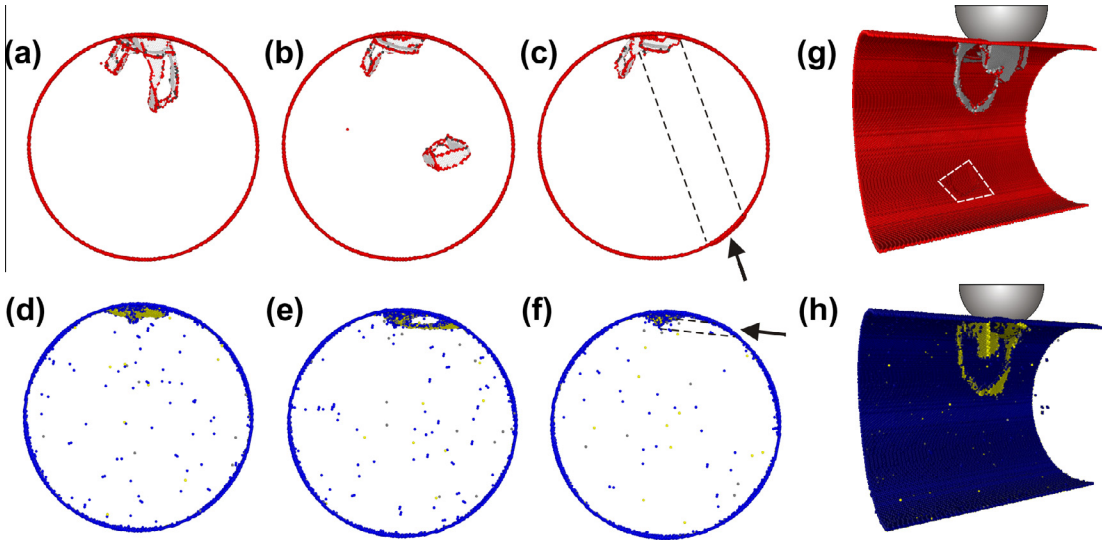

Fig. 6. MD simulations of spherical indentation in [1 1 1]-oriented single-crystalline fcc NWs. (a)–(c) Nucleation, propagation and escape of a prismatic dislocation loop during a single yield event in Ni NWs. (d)–(f) Emission and escape of a single-arm dislocation localized near the tip–NW contact in Au NWs. Spherical tip in the upper region is not shown. Deformation microstructures obtained with a contact depth of 1.8 nm in (g) Ni NW and (h) Au NW. Bottom area highlighted by a dashed line in (g) represents the free surface zone where prismatic loops have escaped during nanoindentation.

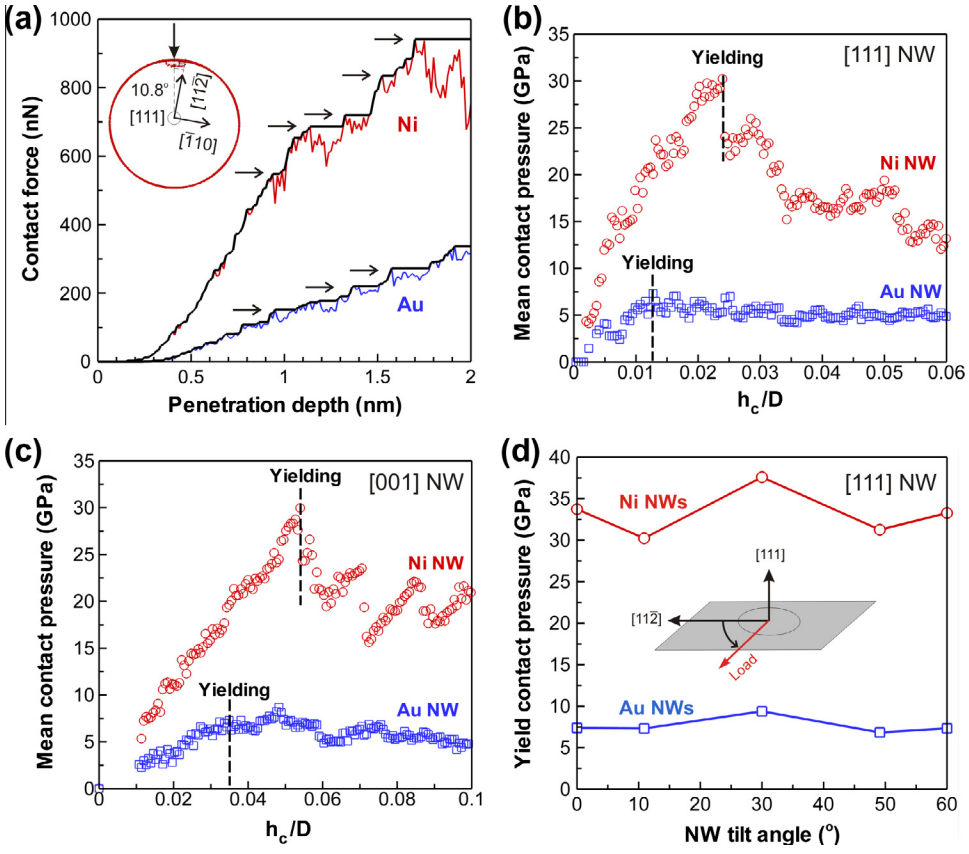

Fig. 7. Hardness of Ni and Au NWs simulated by MD. (a) Contact force evolution as a function of penetration depth with crystal orientations shown in inset. Each horizontal arrow indicates a single yield event. Effects of SFE on mean contact pressure in (b) [1 1 1]-oriented NWs and (c) [0 0 1]-oriented NWs. (d) Change in contact pressure at initial yield point as a function of NW tilt angle with respect to the [1 1 $\bar{2}$] crystallographic direction in [1 1 1]-oriented Ni NWs.

shown in Fig. 4 are in the determination of the contact depth h_c from digital image analysis of indentation marks left in the NW surface, which could be as high as 10% for large contact depths due to the plastic pile-ups, and the diameter variations if the NW did not perfectly adhere to the substrate, although this error was found to be to

<5% in this study, including the variation due to the irregular pores in the template. Furthermore, if we assume a random orientation of NWs from drop-casting, the atomistic simulation results presented in Fig. 7b and d give confidence that the NW orientation had little effect on the experimentally determined hardness properties of bimetallic NWs. Rather, we found that the size and SFE of the materials played a larger role in the nanoindentation response and plastic behavior of the NWs.

4.2. Nanoindentation size effects

To understand the fundamental role that SFE plays on the ISE in bimetallic NWs, we compared the hardness data in Fig. 4a to the classic Nix–Gao relation [64] predicting the change in microhardness H with the contact depth h_c such that:

$$\left(\frac{H}{H_0}\right)^2 = 1 + \frac{h^*}{h_c}, \tag{3}$$

where h^* is a characteristic length scale that generally depends on not only the properties of the indented material but also on the indenter angle, and is typically of the order of micrometers [80]. H_0 is the size-independent hardness obtained for large depths ($h_c \gg h^*$). A priori, the ISE observed in our AFM experiments should be influenced by the material properties only since the cube-corner tip geometry was constant. However, an initial fitting of experimental and atomistic simulation results tended to work poorly and yielded unreasonable values for H_0 and h^* compared to literature values for thin films and coatings in Ni and Au [81–84]. This was attributed to the fact that the plasticity of nanoindented NWs is governed by discrete dislocation bursts rather than a continuous plastic flow, suggesting that the Nix–Gao relation used could either break down at small indentation depths [85] or be associated with a SFE-independent characteristic length scale h^*.

We verified the latter hypothesis by assigning the parameter h^* in the Nix–Gao relation as the diameter of the largest NW, which represents the physical limit for the extension of the plastic zone. Using this assumption, Fig. 4a shows an excellent fit between hardness data and the Nix–Gao relation for both Ni segments and Au segments when fitting values for H_0 are equal to 2.97 and 1.09 GPa, respectively. These H_0 values are also significantly closer to those reported for nanoindentation of Ni and Au thin films mentioned above. In summary, this analysis suggests that ISE observed in bimetallic Ni–Au NWs are material independent and primarily linked to the NW diameter.

4.3. NW hardness dependence on material properties

Following the analysis of Rester et al. [86], the nanohardness H_0 may be a function of the SFE, the shear modulus G, the magnitude of the Burgers vector b, and possibly the initial dislocation density. While having an initial dislocation density was found possible in electrodeposited metallic NWs [87,88], the densities between the different metals should be of the same order of magnitude, and thus should be considered inconsequential in terms of the mechanical behavior in nanoindentation, as suggested in the work by Rester. Furthermore, if electrodeposited metallic NWs have an initial dislocation density, it is statistically unlikely to be high enough to affect more than a few of our data points, with the exception of occasional bent Au segments, which were probably plastically deformed. Also, as a measure of control, we avoided indentations <1 μm from a bent zone to minimize the potential effects of dislocation densities.

In order to better understand the effects of material properties on nanohardness [64], we normalized H by the product $G \times b$ and the SFE as shown in Fig. 4b and c, respectively. It is worth noting from the material properties presented in Table 1 that both G and SFE exhibit the same 3-fold increase between Au and Ni metals, while b remains almost constant. Therefore, Fig. 4b and c allows us to conclude that the measured hardness is mostly dependent on the shear modulus and SFE. It is interesting to note, however, that the normalized H values predicted by the present atomistic simulations with pristine NWs are somewhat different in Fig. 4b when normalized by $G \times b$. Nevertheless, the hardness data beyond the initial yielding zone tend to a better convergence when normalized by the SFE in Fig. 4c. This observation is consistent with the difference in yielding mechanisms due to the SFE shown in Fig. 6, suggesting that the hardness is largely governed by the SFE at high applied plastic strains.

4.4. Hardness dependence on NW diameter

Fig. 4a points to two possible regimes of diameter-dependent hardness in bimetallic NWs, as a function of the normalized contact depth imposed by the tip. First, an initial yielding regime is predicted by MD simulations for $2\% \leqslant h_c/D \leqslant 5\%$, a range in which the plastic behavior of pristine, defect-free Ni NW segments is associated with the nucleation of dislocation loops and their absorption on opposite surfaces, as shown in Fig. 6a and c. The range of contact depths corresponding to this regime is highlighted in grey in Fig. 4a for clarity. Interestingly, Fig. 4a shows that one portion of hardness measurements in Ni NW segments lies in the initial yielding regime, whereas the other portion is outside. Prior to the first yielding event, surface dislocation sources manifest themselves by the presence of GNDs under the nanoindentation tip. Under these

Table 1
Material properties of Ni and Au metals used in Fig. 4b and c [36].

Metal	SFE (mJ m^{-2})	G (GPa)	b (nm)
Ni	123.6	76	0.249
Au	41.6	27	0.288

conditions, the study of Jennings et al. [89] demonstrated that the stress required to emit new lattice dislocations from surface sources is strongly strain rate sensitive, and leads to a reduced dependence on sample diameter as the imposed strain rate decreases. A log–log representation of our hardness vs. diameter data in Fig. 8a for Ni NW segments deformed with $h_c/D < 5\%$ supports this theory. More specifically, fcc metal nanopillars and NWs are understood to behave with an inverse relationship between strength and diameter according to a power-law scaling of the type D^{-n} with n typically varying between 0.4 and 1.0 [90,91]. However, this group of hardness measurements tends to exhibit a power-law scaling exponent of $n = 0.18$, significantly smaller than the values reported above. In addition, it is worth noting that the statistical hardness distribution appears to be large, which qualitatively agrees with the occurrence of thermally activated processes and a minimum energy barrier for surface dislocation nucleation.

Second, Fig. 8a also shows that Ni NW segments exhibit a size dependence with a power-law scaling exponent of $n = 0.80$ when only the data falling outside the initial yielding regime, i.e. obtained with $h_c/D \approx 5$–7%, are considered.

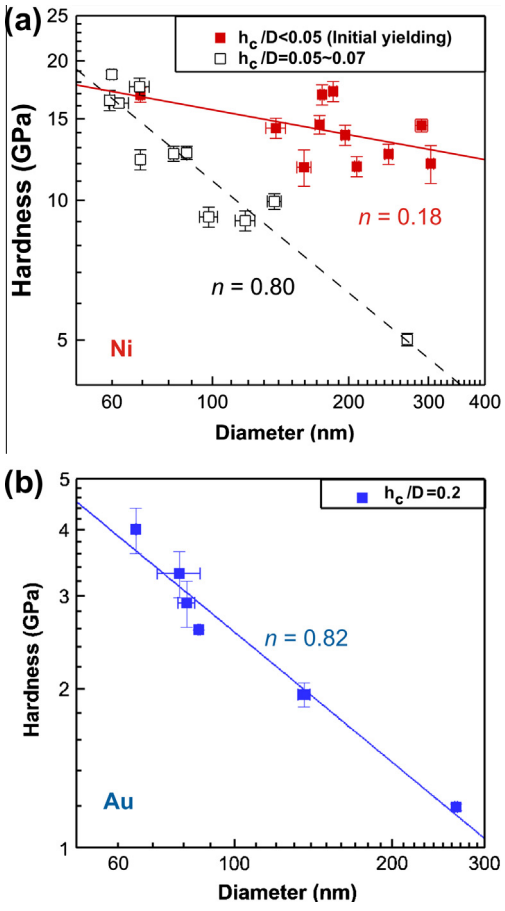

Fig. 8. Power-law scaling of experimental hardness data with diameter in bimetallic NWs. (a) Ni NW segments with normalized contact depths <5% (solid symbols) and between 5% and 7% (open symbols). (b) Au NW segments with normalized contact depths ~20%.

This result is in better agreement with the scaling exponents reported in the literature, and suggests that the plastic deformation process in this case is associated with collective dislocation dynamics such as dislocation–dislocation interactions and dislocation multiplications, rather than surface dislocation nucleation. Our MD simulations have shown that this hypothesis is possible in the nanoindentation of Ni NWs with certain tilt rotations when newly nucleated dislocations are blocked at the bottom boundary, thereby increasing the probability that immobile defects are present in the crystal at large contact depths.

Furthermore, Fig. 4a shows that all hardness measurements in Au NW segments appear to fall chiefly outside the initial yield regime predicted by MD simulations. Fig. 8b presents a log–log plot of our hardness measurements in Au NW segments with $h_c/D \approx 15$–20%, showing a power-law scaling equal to $n = 0.82$ (we note that $n = 0.80$ was also found for other sets in Au segments at smaller and larger normalized contact depths). This phenomenon could be attributed to the prestraining of several Au segments that were found to be plastically bent after synthesis as shown in Fig. 2c, presumably containing defects. Another possibility suggested by the MD simulation snapshots in Fig. 7 is that the SFE affects the interaction processes between newly nucleated dislocation loops and free surfaces. For Ni NW segments, it is possible to assume that the high SFE is responsible for confining the size of the loops inside the crystal, which promotes slip localization. In turn, dislocations resulting from localized slip in fcc metal NWs is more easily absorbed by opposite surfaces due to image forces [92]. On the contrary, the low SFE in Au segments allows the dislocation loop to expand across the NW cross-section, truncating the dislocation arms, and thereby favoring the interaction with other crystal defects, more consistent with the idea of a collective dislocation behavior. However, the lack of experimental measurements in Au NW segments with shallow indentations at $h_c/D < 5\%$ precludes drawing a decisive conclusion. Nevertheless, our experiments yield some additional insight by suggesting that the SFE has limited influence on the collective dislocation dynamics and corresponding size dependence, similar to the reports on micropillar compression of a vast range of fcc metals.

5. Conclusion

An experimental approach using AFM nanoindentation was successfully developed to examine the local plasticity and size-dependent hardness of bimetallic Ni–Au NWs with small dimensions attached to chemically functionalized flat substrates. Template-assisted electrodeposition was used to prepare single-crystalline bimetallic NWs with a growth direction of either [1 1 1] or [0 0 1]. The structure of these NMs was found to be stable during long-term aging, while the presence of oxide did not appear to affect the hardness of Ni NW segments. The hardness of individual NW segments was found to be larger in Ni than in Au

owing to the difference in SFE and shear modulus between these two metals; however, a major finding predicted by MD simulations was that the interaction mechanisms between newly emitted dislocations and free surface were fundamentally different between Ni and Au single-crystalline NWs. Furthermore, we have demonstrated that the ISE observed in bimetallic Ni–Au NWs subjected to nanoindentation was primarily SFE independent and only related to the geometrical limit imposed by the NW diameter on the plastic zone. The SFE was found to have limited influence on the power-law diameter dependence of hardness of Au and Ni NW segments at large plastic deformation. Remarkably, however, the initial yielding of NW segments associated with the emission dislocation loops from surface sources was found to exhibit little-to-no diameter dependence. This combined experimental–atomistic simulation study therefore provides new insight into the size effects on surface-mediated plasticity of geometrically confined fcc metals, which is critically important for understanding the mechanical behavior of NW-based functional devices.

Acknowledgements

E.W. and F.S. gratefully thank support from the National Science Foundation (NSF) CAREER Program (DMR-0747658) and the computational resources provided by the Vermont Advanced Computing Center, which is supported by NASA (NNX-08AO96G). J.M.H. acknowledges support from the NSF (EAR-0922961) for purchase of the X-ray powder diffractometer. T.A. thanks the Undergraduate Research Endeavors Competitive Award (URECA) from the University of Vermont and the NASA Vermont Space Grant Consortium. The authors would also like to thank Mr. Daniel Merkel for contributions in the SEM and EDS characterization of bimetallic NWs. The software LAMMPS was developed by Plimpton [93] with funding from the US Department of Energy.

Appendix A. Supplementary material

Supplementary data associated with this article can be found, in the online version, at http://dx.doi.org/10.1016/j.actamat.2013.11.067.

References

[1] Samardak A, Sukovatitsina E, Ognev A, Chebotkevich L, Mahmoodi R, Peighambari S, et al. High-density nickel nanowire arrays for data storage applications. JPCS, vol. 345. Bristol: IOP Publishing; 2012. p. 012011.
[2] Lee S-H, Jung Y, Agarwal R. Nat Nanotechnol 2007;2:626.
[3] Rex M, Hernandez FE, Campiglia AD. Anal Chem Anal Chem 2006;78:445.
[4] Haes AJ, Stuart DA, Nie S, Van Duyne RP. J Fluoresc 2004;14:355.
[5] Cui Y, Wei Q, Park H, Lieber CM. Science 2001;293:1289.
[6] Sudeep P, Joseph SS, Thomas KG. J Am Chem Soc 2005;127:6516.
[7] Salem AK, Searson PC, Leong KW. Nat Mater 2003;2:668.
[8] Amir Parviz B, Ryan D, Whitesides GM. IEEE Trans Adv Pack 2003;26:233.
[9] Liu X, Wang D, Li Y. Nano Today 2012.
[10] Tok JBH, Chuang F, Kao MC, Rose KA, Pannu SS, Sha MY, et al. Angew Chem Int Ed 2006;45:6900.
[11] Keating CD, Natan MJ. Adv Mater 2003;15:451.
[12] Nicewarner-Pena SR, Freeman RG, Reiss BD, He L, Peña DJ, Walton ID, et al. Science 2001;294:137.
[13] Walton ID, Norton SM, Balasingham A, He L, Oviso DF, Gupta D, et al. Anal Chem Anal Chem 2002;74:2240.
[14] Link S, El-Sayed MA. J Phys Chem B 1999;103:4212.
[15] Diao J, Gall K, Dunn ML, Zimmerman JA. Acta Mater 2006;54:643.
[16] Liang H, Upmanyu M, Huang H. Phys Rev B 2005;71:241403.
[17] Lucas M, Leach AM, McDowell MT, Hunyadi SE, Gall K, Murphy CJ, et al. Phys Rev B 2008;77:245420.
[18] Weinberger CR, Jennings AT, Kang K, Greer JR. J Mech Phys Solid 2012;60:84.
[19] Wang F, Liu Y, Yin X, Wang N, Wang D, Gao Y, et al. J Appl Phys 2010;108:074311.
[20] Branicio PS, Rino J-P. Phys Rev B 2000;62:16950.
[21] Han J, Fang L, Sun J, Han Y, Sun K. J Appl Phys 2012;112:114314.
[22] Zhu T, Li J, Samanta A, Leach A, Gall K. Phys Rev Lett 2008;100:025502.
[23] Wood EL, Sansoz F. Nanoscale 2012;4:5268.
[24] Park HS, Klein PA. Phys Rev B 2007;75:085408.
[25] Wang JW, Sansoz F, Huang JY, Liu Y, Sun SH, Zhang Z, et al. Nat Commun 2013;4.
[26] Zheng H, Cao AJ, Weinberger CR, Huang JY, Du K, Wang JB, et al. Nat Commun 2010;1.
[27] Zheng H, Wang JB, Huang JY, Cao AJ, Mao SX. Phys Rev Lett 2012;109.
[28] Seo J-H, Yoo Y, Park N-Y, Yoon S-W, Lee H, Han S, et al. Nano Lett 2011;11:3499.
[29] Lu Y, Huang JY, Wang C, Sun SH, Lou J. Nat Nanotechnol 2010;5:218.
[30] Lu Y, Song J, Huang JY, Lou J. Nano Res 2011;4:1261.
[31] Lu Y, Song J, Huang JY, Lou J. Adv Funct Mater 2011;21:3982.
[32] Deng C, Sansoz F. Appl Phys Lett 2009;95:091914.
[33] Deng C, Sansoz F. Nano Lett 2009;9:1517.
[34] Deng C, Sansoz F. ACS Nano 2009;3:3001.
[35] Deng C, Sansoz F. Phys Rev B 2010;81:155430.
[36] Deng C, Sansoz F. Acta Mater 2009;57:6090.
[37] Jiang J-W, Leach AM, Gall K, Park HS, Rabczuk T. J Mech Phys Solid 2013;61:1915.
[38] Wu B, Heidelberg A, Boland JJ. Nat Mater 2005;4:525.
[39] Legros M, Gianola D, Motz C. MRS Bull 2010;35.
[40] Yue Y, Liu P, Zhang Z, Han X, Ma E. Nano Lett 2011;11:3151.
[41] Gianola DS, Sedlmayr A, Monig R, Volkert CA, Major RC, Cyrankowski E, et al. Rev Sci Instrum 2011;82:063901.
[42] Peng C, Zhan Y, Lou J. Small 2012;8:1889.
[43] Mompiou F, Legros M, Sedlmayr A, Gianola DS, Caillard D, Kraft O. Acta Mater 2012;60:977.
[44] Kiener D, Hosemann P, Maloy S, Minor A. Nat Mater 2011;10:608.
[45] Lu Y, Peng C, Ganesan Y, Huang JY, Lou J. Nanotechnology 2011;22:355702.
[46] Dou R, Derby B. Scripta Mater 2008;59:151.
[47] Mordehai D, Lee S-W, Backes B, Srolovitz DJ, Nix WD, Rabkin E. Acta Mater 2011;59:5202.
[48] Wang Z, Mook WM, Niederberger C, Ghisleni R, Philippe L, Michler J. Nano Lett 2012;12:2289.
[49] Uchic MD, Dimiduk DM, Florando JN, Nix WD. Science 2004;305:986.
[50] Rinaldi A, Peralta P, Friesen C, Sieradzki K. Acta Mater 2008;56:511.
[51] Wu B, Heidelberg A, Boland JJ, Sader JE, Sun Li. Nano Lett 2006;6:468.
[52] Cimalla V, Röhlig C-C, Pezoldt J, Niebelschütz M, Ambacher O, Brückner K, et al. J Nanomater 2008;2008:44.

[53] Zhang H, Tang J, Zhang L, An B, Qin L-C. Appl Phys Lett 2008;92:173121.
[54] Oliver WC, Pharr GM. J Mater Res 1992;7:1564.
[55] Choi Y, Van Vliet KJ, Li J, Suresh S. J Appl Phys 2003;94:6050.
[56] Mordehai D, Kazakevich M, Srolovitz DJ, Rabkin E. Acta Mater 2011;59:2309.
[57] Soifer YM, Verdyan A, Kazakevich M, Rabkin E. Mater Lett 2005;59:1434.
[58] Gouldstone A, Koh HJ, Zeng KY, Giannakopoulos AE, Suresh S. Acta Mater 2000;48:2277.
[59] Bansal S, Toimil-Molares E, Saxena A, Tummala RR. Nanoindentation of single crystal and polycrystalline copper nanowires. In: Proc 55th ELEC COMP C, 2005. IEEE; 2005. p. 71.
[60] Feng G, Nix WD, Yoon Y, Lee CJ. J Appl Phys 2006;99:074304.
[61] Li X, Gao H, Murphy CJ, Caswell KK. Nano Lett 2003;3:1495.
[62] Minor A, Morris J, Stach E. Appl Phys Lett 2001;79:1625.
[63] McAllister QP, Gillespie Jr JW, VanLandingham MR. J Mater Res 2012;27:197.
[64] Nix WD, Gao HJ. J Mech Phys Solid 1998;46:411.
[65] Dupont V, Sansoz F. J Mater Res 2009;24:948.
[66] Sansoz F, Dupont V. Scripta Mater 2010;63:1136.
[67] Lian J, Wang J, Kim Y-Y, Greer J. J Mech Phys Solid 2009;57:812.
[68] Bauer LA, Reich DH, Meyer GJ. Langmuir 2003;19:7043.
[69] Cortés A, Riveros G, Palma JL, Denardin JC, Marotti RE, Dalchiele EA, et al. J Nanosci Nanotechnol 2009;9:1992.
[70] Daniel M-C, Astruc D. Chem Rev 2003;104:293.
[71] Sansoz F, Gang T. Ultramicroscopy 2010;111:11.
[72] Nečas D, Klapetek P. Cent Eur J Phys 2012;10:181.
[73] Mishin Y, Farkas D, Mehl MJ, Papaconstantopoulos DA. Phys Rev B 1999;59:3393.
[74] Grochola G, Russo SP, Snook IK. J Chem Phys 2005;123:204719.
[75] Ackland GJ, Jones AP. Phys Rev B 2006;73:054104.
[76] Feng G, Nix WD, Yoon Y, Lee CJ. J Appl Phys 2006;99.
[77] Sansoz F, Stevenson KD. Phys Rev B 2011;83:224101.
[78] McAllister QP, Gillespie JWJ, VanLandingham MR. J Mater Res 2012;27:197.
[79] Askari D, Feng G. J Mater Res 2012;27:586.
[80] Qu S, Huang Y, Nix WD, Jiang H, Zhang F, Hwang KC. J Mater Res 2004;19:3423.
[81] Zong Z, Lou J, Adewoye O, Elmustafa A, Hammad F, Soboyejo W. Mater Sci Eng A 2006;434:178.
[82] Graça S, Colaço R, Vilar R. Surf Coat Technol 2007;202:538.
[83] Dietiker M, Nyilas RD, Solenthaler C, Spolenak R. Acta Mater 2008;56:3887.
[84] Ma Z, Long S, Pan Y, Zhou Y. J Appl Phys 2008;103:043512.
[85] Greer JR, Oliver WC, Nix WD. Acta Mater 2005;53:1821.
[86] Rester M, Motz C, Pippan R. Scripta Mater 2008;58:187.
[87] Karim S, Toimil-Molares ME, Maurer F, Miehe G, Ensinger W, Liu J, et al. Appl Phys A 2006;84:403.
[88] Tian M, Wang J, Kurtz J, Mallouk TE, Chan M. Nano Lett 2003;3:919.
[89] Jennings AT, Li J, Greer JR. Acta Mater 2011;59:5627.
[90] Dou R, Derby B. Scripta Mater 2009;61:524.
[91] Sansoz F. Acta Mater 2011;59:3364.
[92] Weinberger CR, Cai W. Proc Natl Acad Sci USA 2008;105:14304.
[93] Plimpton J. J Comp Phys 1995;117:1.